MATERIALS SCIENCE

Radiolytic redox interplay defines nanomaterial synthesis in liquids

Auwais Ahmed, Erik C. Boyle, Peter A. Kottke, Andrei G. Fedorov*

Irradiation of a liquid solution generates solvated electrons and radiolysis products, which can lead to material deposition or etching. The chemical environment dictates the dominant reactions. Radiolysis-induced reactions in salt solutions have substantially different results in pure water versus water-ammonia, which extends the lifetime of solvated electrons. We investigate the interplay between transport and solution chemistry via the example of solid silver formation from e-beam irradiation of silver nitrate solutions in water and water-ammonia. The addition of ammonia results in the formation of a secondary ring-shaped deposit tens of micrometers in diameter (formed over tens of seconds) around the primary point of deposition (formed over milliseconds). Simulations uncover the relative importance of oxidizing and reducing reactions and transport effects. Our explanation of this behavior involves mechanisms beyond ammonia's role in extending solvated electron lifetimes.

INTRODUCTION

Electron beam and matter interactions lead to very interesting chemistry on micro- and nanoscales (*1*). Electron-mediated chemistry in the liquid phase is an important problem that has applications in fields such as focused electron beam–induced deposition (FEBID) and nanoparticle synthesis and aggregation (*2*, *3*). These applications are key steps in the further development of control over matter on ever-smaller length and time scales, which is an engine for technological progress. Direct writing of nanoscale structures with FEBID is a promising route to atom-by-atom creation of complex three-dimensional (3D) nanostructures (*4*). It has the potential for exquisite control of topological structure and chemical composition in three dimensions down to atomic scales. Performing FEBID in liquid-phase precursors removes the roadblock of low deposition rates and allows the use of unique synthesis chemistries. Complementary to focused electron beam nanomaterial synthesis are plasma-based techniques that also exploit electron interactions in solutions for improved control of structure and reactivity of nanocatalysts for emerging energy conversion applications (*5*). These are techniques for inducing electrochemistry without electrodes, which allow new angles from which to revisit the basics of electrochemistry and the ability to realize/accelerate reactions (e.g., formation of multicomponent alloys with accurate control of composition and phase) that are difficult or impossible in conventional electrochemistry. Common to these applications is the requirement to understand and control the nature and extent of interactions between electrons, their environment, and other reacting species. The practical realization of these tantalizing possibilities requires the fundamental understanding of solvated electron-mediated redox chemistry and its interplay with reacting species transport. Despite the ability to focus an electron beam down to the nanometer scale at high energies, solid deposition occurs on the micrometer scale (*6*). This length scale is dictated both by the extent of penetration of low-energy electrons and by radiolysis chemistry and transport (*7*, *8*). The dominant processes have been studied for several aqueous solvent systems (*9*–*11*). The addition of ammonia has been demonstrated to provide unusual stability in holding electrons in solution (*12*, *13*). This stability is implicated in the ease of silver nanoparticle synthesis in water-ammonia solutions while markedly increasing system chemical reaction and transport complexity.

The impact of ammonia on the formation of different shapes of deposits and the spatial-temporal dependence of the deposition rate is the new insight we present in this work. In particular, the role of solvated electrons and their interactions with other radiolytic species, as well as the transport of these species within the region of electron beam influence, are not well understood. Previously, it has been shown that Ag nanostructures can be created from irradiation of an aqueous solution of $AgNO_3$ with a high-energy electron beam (*14*). As the reducing radiolytic species reduce Ag ions and complexes, a parallel process of oxidation occurs. The interplay of these oxidizing and reducing pathways determines the size, location, and structure of the produced nanomaterials.

The morphology and deposition rates of created nanostructures are known to depend on the local pH of the solution. A higher pH leads to an increase in the ratio of reducing to oxidizing species (*15*). This leads to aggregation and agglomeration of metallic nanostructures in higher pH environments and dissolution at lower pH. In addition, pH affects the crystallinity of metallic deposits, with increasing pH leading to more crystalline deposits (*14*).

In this work (Fig. 1), we demonstrate that ammonia is useful as a mediator of the behavior of different radiolytic species, particularly in changing the role of hydrogen peroxide from a strong oxidizer (purely aqueous) to a strong reducer (water-ammonia). This results in substantially different deposit morphologies, i.e., ring formation in addition to a central pillar as observed in purely aqueous solutions. We explain this behavior through complementary experiments and first-principles reaction-diffusion simulations of electron beam–induced deposition of Ag in a water-ammonia system.

In water, $AgNO_3$ dissociates into Ag^+ and NO_3^-. Under electron beam irradiation, a process of radiolysis takes place, resulting in the creation of solvated electrons (e_{sol}^-), $H^\bullet$, H_2, $OH^\bullet$, H_2O_2, HO_3^+, and $HO_2^\bullet$ as primary radiolysis species (*16*). These species react with one another and the solution to form secondary radiolysis species such as O_2. The species of greatest significance for synthesis of Ag nanomaterials are the ones that either reduce Ag^+ to Ag or oxidize Ag toAg^+. As shown in Fig. 1A, e_{sol}^- and $H^\bullet$ are the reducing species for

George W. Woodruff School of Mechanical Engineering, Georgia Institute of Technology, 771 Ferst Dr NW, Atlanta, GA 30332, USA.
*Corresponding author. Email: agf@gatech.edu

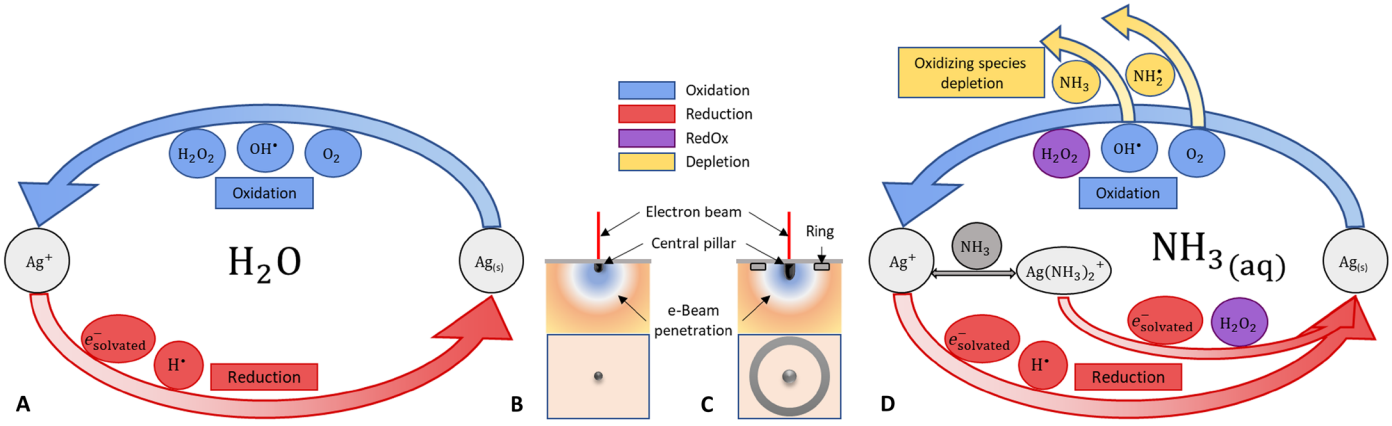

Fig. 1. Overview of deposition process. Important radiolysis products and their roles as oxidizing and reducing species involved in Ag deposition from an $AgNO_3$ precursor in (**A**) water and (**D**) water-ammonia solvents. In the presence of NH_3, Ag^+ ions can form the diamine silver complex $Ag(NH_3)_2^+$, enabling additional reduction pathways. The role of H_2O_2 is altered from purely oxidizing in water to both oxidizing Ag and reducing $Ag(NH_3)_2^+$ in water-ammonia. Furthermore, reactions with NH_3 and $NH_2^{\bullet}$ deplete $OH^{\bullet}$ and O_2, suppressing the oxidation rate of Ag. (**B** and **C**) A schematic of the deposition process in (B) water and (C) water-ammonia, showing the broadening of the central pillar deposit and the appearance of a ring deposit in water-ammonia.

Ag^+, while H_2O_2, O_2, and $OH^{\bullet}$ are species oxidizing Ag. At any point in space and time, the creation of an Ag solid phase is only possible if the rate of reduction is higher than the rate of oxidation. In the case of the water-$AgNO_3$ system, a net-reducing environment exists only at the point where electron beam interacts with solution, resulting in the creation of central pillar, as shown in Fig. 1. The rate of deposition is diminished by the presence of oxidizing species, such that only in a very small region near the electron beam impingement point can solid formation occur. The use of an aqueous ammonia solvent for $AgNO_3$ leads to a notable change in chemical behavior. The presence of ammonia in an aqueous solution triggers the formation of diamine silver ion complexes, $Ag(NH_3)_2^+$, from Ag ions (Eq. 1). This reversible reaction strongly favors the formation of $Ag(NH_3)_2^+$, to the extent that free Ag^+ concentrations are negligibly small for sufficiently high concentrations of ammonia. $Ag(NH_3)_2^+$ can be reduced by e^-_{sol}, via Eq. 2, to form metallic Ag

$$Ag^+ + 2NH_{3(aq)} \rightleftharpoons Ag(NH_3)_2^+ \quad (1)$$

$$Ag(NH_3)_2^+ + e^-_{sol} \rightarrow Ag + 2NH_3 \quad (2)$$

$Ag(NH_3)_2^+$ can also be reduced by H_2O_2 to produce Ag. In the case of an $AgNO_3$ solution in pure water, this reduction mechanism is absent, and H_2O_2 is only an oxidizer of Ag

$$2Ag(NH_3)_2^+ + H_2O_2 \rightarrow 2Ag + 2NH_3 + H_2O + 1/2\,O_2 \quad (3)$$

This means that the use of a water-ammonia solvent leads to a role reversal for H_2O_2 from solely an oxidizer to a reducer as well as an oxidizer. Consumption of H_2O_2 in the reduction of $Ag(NH_3)_2^+$ leads to a decrease in the rate of Ag oxidation. Radiolysis of aqueous ammonia also creates additional chemical pathways that mediate Ag/Ag^+ redox chemistry through the production of species such as $NH_2^{\bullet}$ and the interaction of radiolysis species with NH_3. Specifically, this leads to consumption of oxidizing species through the following reactions

$$NH_{3(aq)} + OH^{\bullet} \rightarrow NH_2^{\bullet} + H_2O \quad (4)$$

$$NH_2^{\bullet} + OH^{\bullet} \rightarrow NH_2OH \quad (5)$$

$$NH_2^{\bullet} + H_2O_2 \rightarrow NHOH + H_2O \quad (6)$$

$$NH_2^{\bullet} + O_{2(aq)} \rightarrow NH_2O_2 \quad (7)$$

$$2NH_2^{\bullet} \rightarrow N_2H_4 \quad (8)$$

$$OH^{\bullet} + N_2H_4 \rightarrow H_2O + N_2H_3^{\bullet} \quad (9)$$

As a result, the concentration of species oxidizing Ag is strongly suppressed in a water-ammonia solvent in comparison to a pure water solvent, making the deposition environment more reducing.

RESULTS

Figure 2 shows the results of experiments for both water and water-ammonia. A central pillar deposit is formed at the point of irradiation in each case. A ring is formed around the central pillar only when the water-ammonia solvent is used (Fig. 2, A to D). The ring increases in diameter with increasing beam energy. Electron beams at 10- and 15-keV energy result in the formation of dendritic structures on the outer edge of the ring. The creation of these dendritic structures can be attributed to Mullins-Sekerka instabilities (*17*, *18*). The imaging process after "spot" mode irradiation cannot explain these deposit formations (see fig. S2).

The addition of ammonia to an aqueous solution increases the pH and introduces new chemistry. To distinguish between the impacts of these two effects, we also test a water solution with its pH elevated to match the water-ammonia solution. To determine whether the deposition behavior in water-ammonia solution is attributable to its high pH, a 1 mM NaOH-water solution with pH 12 was irradiated with a 30-keV electron beam. Rings were not formed in pure water regardless of pH (Fig. 2, E and F). This shows that the unusual deposition behavior in the water-ammonia solvent is not due to its elevated pH and requires an alternative explanation.

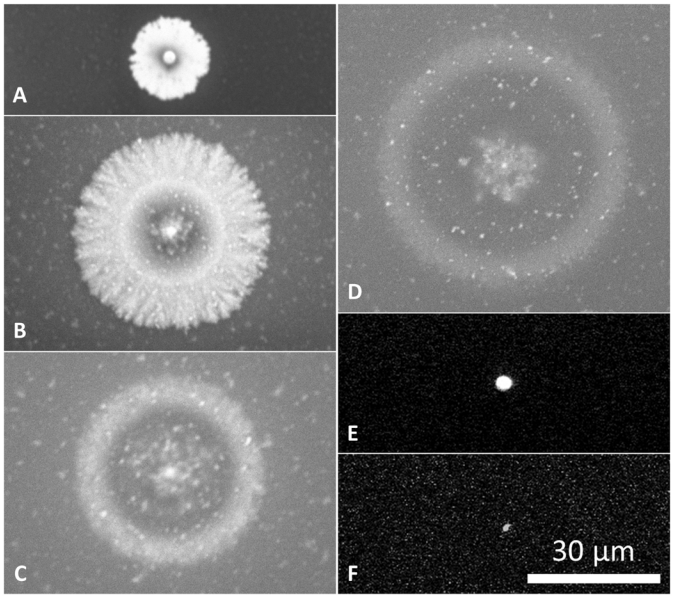

Fig. 2. Deposition results. Deposition in "spot" mode, (**A** to **D**) 1 mM $AgNO_3$, 30% (v/v) NH_3 aqueous solution, and (**E** and **F**) 1 mM $AgNO_3$ aqueous solution. (A) 10-keV, (B) 15-keV, (C) 20-keV, and (D) 30-keV beam energy. A central deposit and small ring are formed. Ring diameter increases with increasing beam energy. At 10 and 15 keV, dendritic structures are formed on the ring. At (E) 30 keV, neutral pH, and (F) 30 keV, pH 12: Deposit was created only at the irradiation site. Exposure time is 30 s for all cases. Imaging is performed with a 30-keV, 2-nA electron beam and an Everhart-Thornley secondary electron detector.

Simulations of the coupled interplay between species transport and the local reaction rates provide a tool to uncover and define the dominant chemical interactions in space and time.

We model the processes in a 2D axisymmetric domain (fig. S1) and solve reaction-diffusion equations (eq. S1) for 1 mM $AgNO_3$ in pure water and water-ammonia solvents. The rate constants incorporated in the simulation are taken from (*8*, *19*) (see the Supplementary Materials). The creation of radiolysis species, their reactions, and transport have been predicted to simulate Ag formation via the net effects of reduction and oxidation pathways, as shown in Fig. 1. An electron beam enters the solution through an electron-transparent polyimide membrane. Electrons then undergo a series of elastic and inelastic collisions with molecules in the solution, triggering a process of radiolysis. The extent of the electron beam penetration in the solution depends on the energy and determines the region in which radiolysis takes place. Figure 3 (A to C), presented at the same scale, shows the spatial distribution of dose rate for electron beams at 30-, 15-, and 10-keV energies, respectively. The concentration of radiolysis species is a function of the spatial dose rate and irradiation time. A change in electron energies affects the spatial and temporal concentrations of radiolysis species, resulting in distinct changes in deposition outcomes. A Monte Carlo simulation, whose results are exemplified in Fig. 3D, was used to model electron trajectories and energy loss within the domain. The combined electron energy loss per unit time due to collisions occurring within a cell defines the local dose rate (source term) in the transport equation for the reaction-diffusion simulations.

Figure 4A depicts dose rate variation in the water-ammonia solution at the membrane, where experimental results are obtained

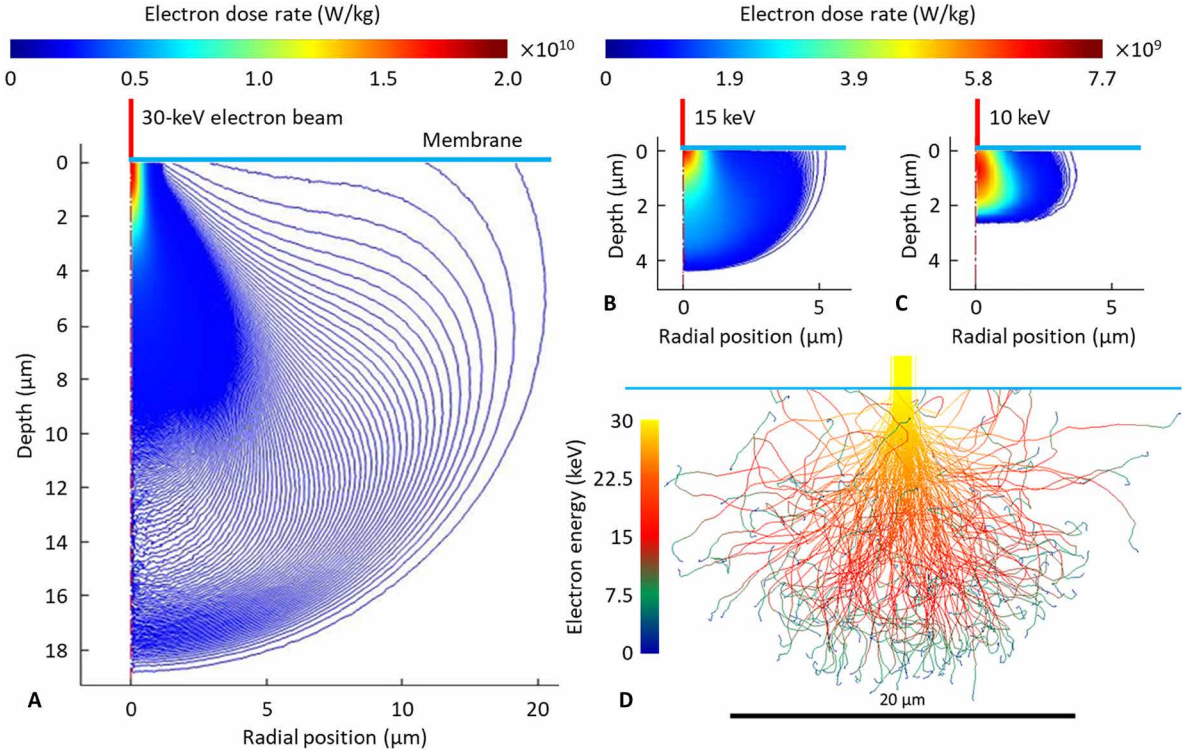

Fig. 3. Electron beam dose rates. The spatial distribution of dose rate is a function of electron beam energy, with a higher beam energy resulting in a larger region of interaction. 2D axisymmetric plots of dose rate for beam energies of (**A**) 30 keV, (**B**) 15 keV, and (**C**) 10 keV in 30% (v/v) NH_3 aqueous solution. (**D**) Electron trajectories extracted from a Monte Carlo simulation (30 keV shown) were used to calculate dose rates.

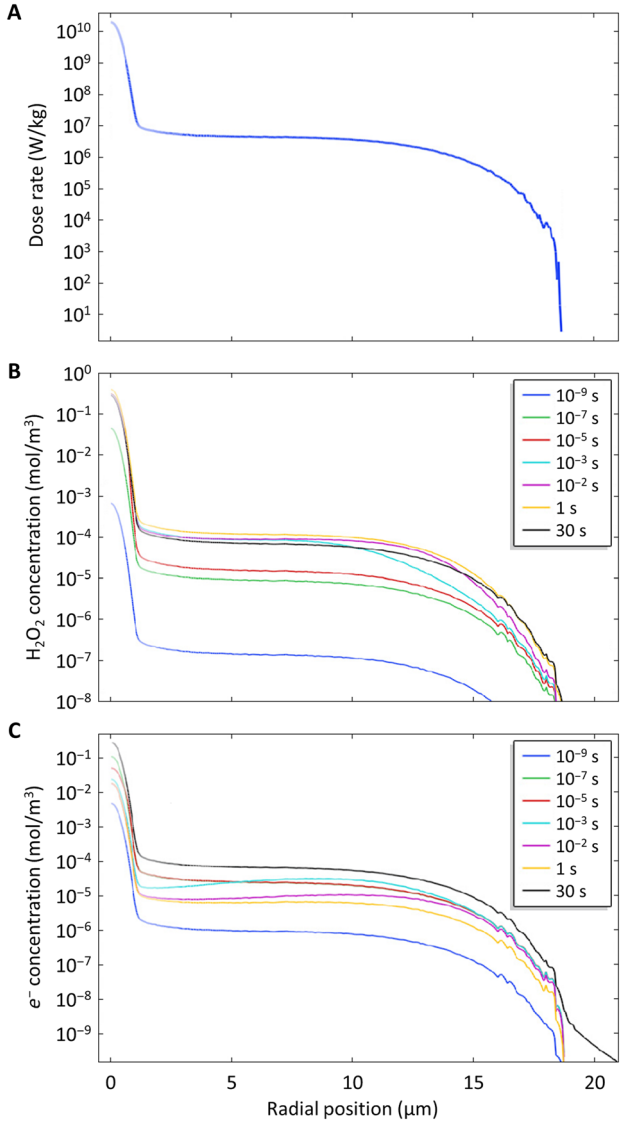

Fig. 4. e-Beam irradiation of water-ammonia. (**A**) Dose rate distribution at the membrane for a 30-keV electron beam in 30% (v/v) aqueous solution. There are two length scales of interest. The first is associated with the region directly irradiated by the electron beam, and the second with the extent of electron penetration inside the solution. (**B**) The concentration profile of H_2O_2 initially follows the dose rate profile. In the beam region, a quasi–steady state concentration is achieved by 10^{-5} s. After attaining its quasi–steady state concentration in the beam region, H_2O_2 continues diffusing into the envelope region, where it reaches a quasi–steady state concentration by around 1 s. (**C**) The concentration of e^-_{sol} increases at short times, and these high concentrations drive the creation of a central pillar. After 10^{-7} s, the concentration of e^-_{sol} in the beam region begins falling.

(Fig. 2). The radial distribution of the electron dose rate displays three domains—a large peak in the dose rate where the primary electron beam enters the domain (the beam region), an extended region of nearly uniform dose rate (the envelope region), and a far field region with negligible dose rate. The boundaries between these domains give two length scales that are important for explaining the experimental results (for a 30-keV beam, these two length scales are ca. 1 and 18 μm, respectively; Fig. 4A).

Figure 4 (B and C) shows the spatial and temporal variation in concentration at the membrane of the two most important species for producing Ag: H_2O_2 and e^-_{sol}. On the smaller length scale of the beam region, the H_2O_2 concentration reaches quasi–steady state at approximately 10^{-5} s. In the envelope region, its concentration continues increasing for much longer before reaching a quasi–steady state around 1 s. Figure 4C shows the behavior for e^-_{sol}. Its concentration continually evolves throughout the entire process. The e^-_{sol} concentration in the beam region initially peaks and then falls before increasing again. This lack of quasi–steady state behavior is due to the consumption of e^-_{sol} through secondary radiolysis species, which are created on much longer time scales than e^-_{sol}.

To better demonstrate the importance of these length and time scales, the reaction rates for the two key pathways involved in the reduction of $Ag(NH_3)_2^+$ in water-ammonia are plotted for a 30-keV beam in Fig. 5A. $Ag(NH_3)_2^+$ is reduced by e^-_{sol} via Eq. 2 and H_2O_2 via Eq. 3. The pathways reducing Ag^+ are negligible because of the almost complete conversion of Ag^+ into $Ag(NH_3)_2^+$. Initially, e^-_{sol} is the primary reducer of $Ag(NH_3)_2^+$ (10^{-7} s; Fig. 5A), but this behavior inverts at longer times, and reduction by H_2O_2 becomes dominant in the quasi–steady state condition (1 to 30 s; Fig. 5A). Figure 5 (B and C) shows the net Ag creation rate by all mechanisms over time for the water-ammonia and pure water solvents, respectively. In both media, we see the presence of a large peak in the beam region, indicating very high rates of net Ag creation. Since e^-_{sol} is the dominant reducing species at very short times, we conclude that the central pillar is produced primarily from Ag^+ (in water) or $Ag(NH_3)_2^+$ (in water-ammonia) reduction by e^-_{sol}.

Outside the beam region, the behaviors of the two solvents markedly diverge. In the pure water system, the net Ag creation rate falls to negligible or negative (oxidizing) values in the entire envelope region. In the water-ammonia system, we see the establishment of a band with well-defined inner and outer edges where the environment remains net reducing. This can be explained through the interaction of reaction and transport effects. Because the dose rate is highest near the center of the domain, the reducing and oxidizing radiolysis species tend to diffuse outward from the beam region. Consumption of the initial $Ag(NH_3)_2^+$ supply in the envelope region causes $Ag(NH_3)_2^+$ to diffuse inward from the bulk. These opposing species fluxes interact near the edge of the envelope region, and because of the water-ammonia solvent, the radiolysis species produce a net-reducing effect. This shows that the ring is formed over longer time scales, and, as shown in Fig. 5A, H_2O_2 is primarily responsible for its creation, in contrast to the central pillar, which is driven by e^-_{sol}. See figs. S3 and S4 for more details of the ring creation process in water-ammonia.

Figure 6 compares the concentrations of the two main oxidizing species, $OH^\bullet$ and O_2, in both the pure water and water-ammonia solvents. This demonstrates the effect described schematically in Fig. 1, as NH_3 and $NH_2^\bullet$ scavenge these oxidizing species in the water-ammonia system, suppressing their concentrations compared to the pure water system. This action is key in enabling the reduction of $Ag(NH_3)_2^+$ by H_2O_2 away from the beam region, leading to the ring formation observed in experiments.

The physics of the process are 3D. Figure 7 shows a simulation of the net rate of Ag production at 1 s in water-ammonia for a 30-keV beam. The region where Ag is produced at quasi–steady state forms a hemispherical shell. The ring seen in the experimental results of Fig. 2 is the manifestation of this shell at the membrane, which acts

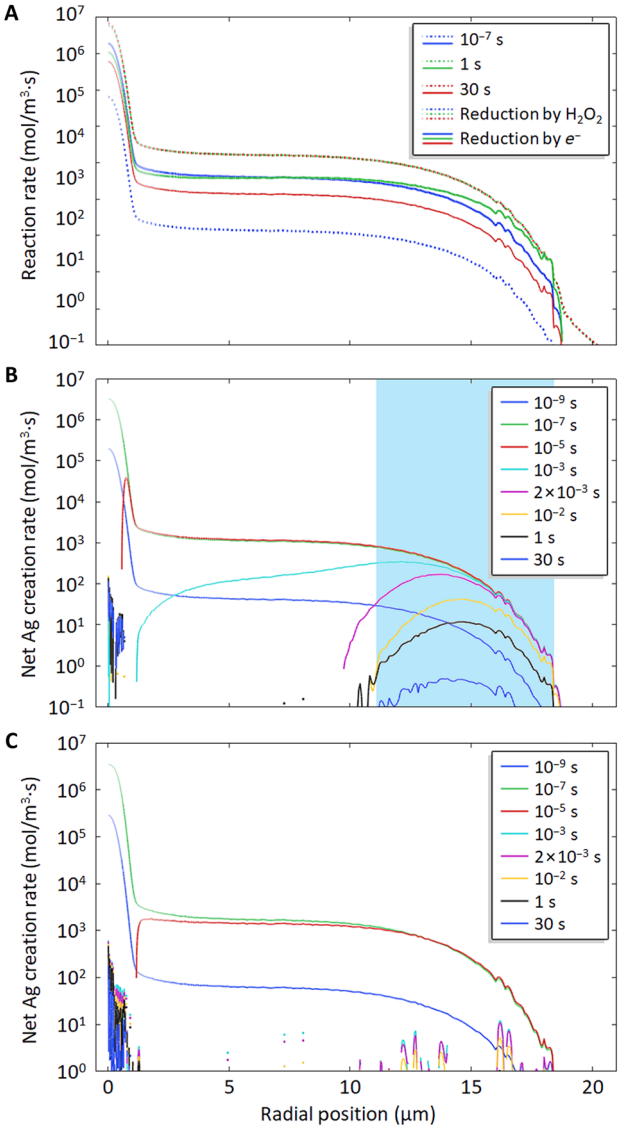

Fig. 5. Water and water-ammonia deposition outcomes. (**A**) Comparison of most important reduction pathways in the creation of Ag in a 30% (v/v) aqueous solution. At short times, reduction of $Ag(NH_3)_2^+$ by e^-_{sol} is dominant, but H_2O_2 becomes dominant at longer times. (**B**) Net rate of Ag creation at membrane by all pathways in a 30% NH_3 (v/v) aqueous solution. Two distinct regions of production are seen—one at the center before 10^{-5} s and one around 15 μm, which persists until times >1 s. The shading highlights the region where ring formation is predicted to occur. (**C**) Net rate of Ag creation at membrane by all pathways in a purely aqueous solution. No production occurs in the bulk beyond 10^{-5} s. A 30-keV electron beam and 1 mM $AgNO_3$ are used for all cases.

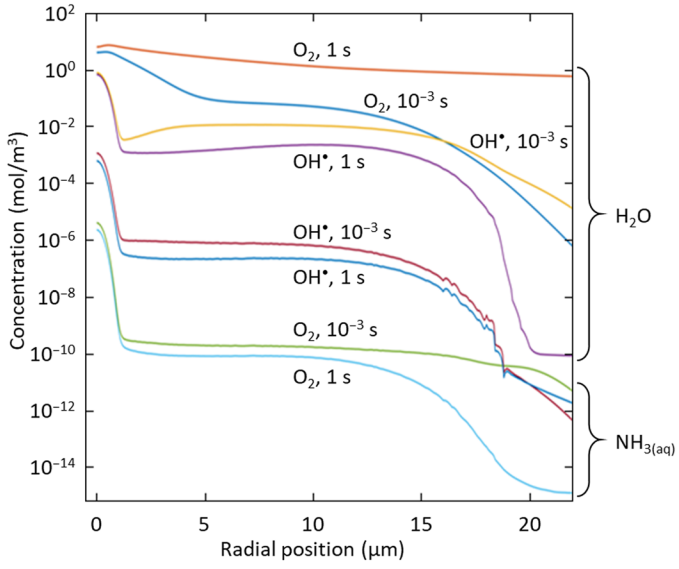

Fig. 6. Suppression of oxidizing species by ammonia. Concentrations of $OH^•$ and O_2 are suppressed in water-ammonia in comparison to pure water because of their scavenging by $NH_2^•$ and NH_3. This creates a highly reducing environment, promoting Ag nanomaterial synthesis in the water-ammonia solution.

as a preferential surface for nucleation. However, the rate of Ag production on the shell is highest in the bulk, away from the membrane. This is attributable to the electrons' greater penetration in the axial direction compared to radially, as shown in the teardrop profile of dose rate in Fig. 3A. This insight is critical for procedures involving the generation of Ag nanoparticles via electron beam interaction, as the region of greatest Ag formation occurs in the bulk solution.

The simulation allows us to predict the expected ring size. As electron energy increases, the region of electron penetration expands further into the bulk. This results in the creation of rings with larger radii. Figure 8 compares the estimated ring locations from simulations to the experimentally measured values (Fig. 2). The model correctly predicts the energy dependence of the ring size. An underprediction of ring size is present, which can largely be attributed to three effects. The first is the electron dose rate distribution. The electron stopping power model available in our Monte Carlo simulation software is known to overpredict electron stopping power (*20*). The second is that we neglect heating by the electron beam (see fig. S5) and convection in the reaction-diffusion simulation. Scaling analysis combined with thermal simulations suggests that the mass diffusion Peclet number, Pe, is, at most, $O(1)$ for the system (see the Supplementary Materials), meaning that thermally induced flow, which would be radially outward from the beam impingement point near the membrane, may have some effect on species distributions (*21*). Both an underprediction of electron transport distance and neglect of species advection would result in an underprediction of ring sizes, especially at higher beam energies. Last, the electron beam interaction with the membrane introduces a radial electric field (*22*, *23*) that could drive electrokinetic flow in the fluid near the membrane surface. If this flow is of sufficient velocity, this would result in changes in species concentration profiles and, therefore, deposition rates with implications for the observed ring locations. Further, to achieve complete quantitative agreement between simulation and experiments, one would also need to account for heterogeneous nucleation and solid-phase formation and motion, which require multiphase simulations. In this work, our focus is on identifying the dominant mechanisms that allow one to explain the interplay between reaction chemistry and species transport, allowing us to correctly predict the trend in experimental behavior.

DISCUSSION

We find the unique behavior of electron beam–induced metal deposition in water-ammonia systems. The mechanisms of radiolytic

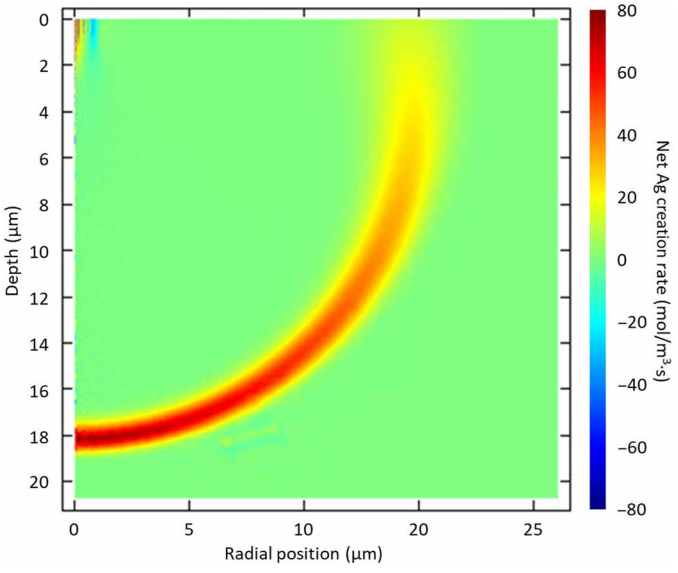

Fig. 7. Regions of Ag production in water-ammonia. Net rate of creation of Ag (difference between reduction and oxidation rates) with irradiation of a 1 mM $AgNO_3$ and 30% (v/v) NH_3 aqueous solution by a 30-keV electron beam at 1 s shown in a 2D axisymmetric domain. There is a positive rate of Ag production at the point of irradiation and in an approximately hemispherical region of the bulk. The small region of a negative creation rate indicates that at this instant and this location, Ag is being consumed by oxidation at a greater rate than it is being produced by reduction of Ag^+ or $Ag(NH_3)_2^+$. In a water system, only the central deposition region of high net Ag production rate is present. The membrane surface provides a preferential location for solid-phase nucleation, which manifests in the creation of a 2D ring as observed in experiments rather than a 3D shell seen in simulations for the water-ammonia system.

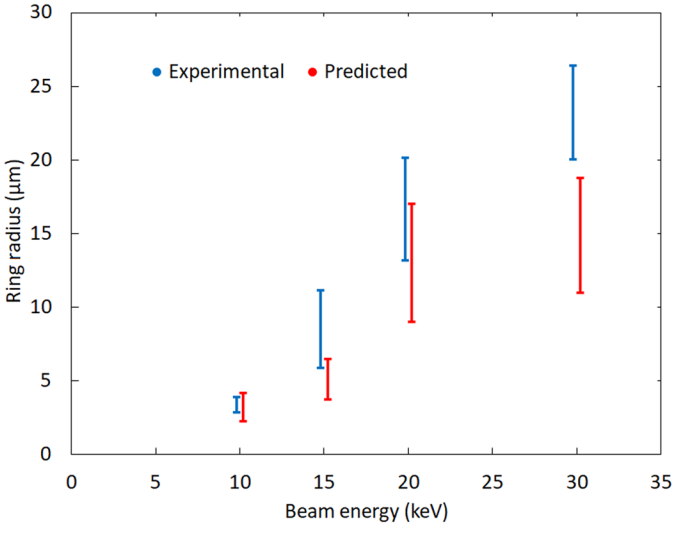

Fig. 8. Experimental and computational ring sizes. Comparison between the experimental observations for the inner and outer diameters of rings and predictions of ring sizes from simulations of the water-ammonia system. For simulated results, the ranges represent the estimated minimum and maximum radii at which the net rate of solid Ag creation exceeds a nominal value—1 mol/m^3·s—at times of 10 ms or greater. This represents the range of positions over which ring deposition is predicted to occur. The size of the ring grows as the beam energy increases. The disagreement arises from the overprediction of stopping power at low electron energies by the Joy-Luo stopping power model used in the simulations.

redox interplay in silver formation from its metal salt solutions are defined through first-principles simulations and supporting experiments. In water-ammonia systems, complex deposition morphologies are observed, with a secondary zone of deposition (ring) created in addition to a commonly observed central pillar at the point of electron beam irradiation. This outcome is attributed to the suppression of oxidizing species in the water-ammonia system via scavenging and the addition of a reduction pathway involving H_2O_2. Simulations highlight the importance of interactions between the dominant reaction pathways and radiolysis species transport for experimentally observed behavior. They show that the central pillar deposition occurs over time scales on the order of microseconds, and solvated electrons are the dominant reducing species at this time scale. The ring creation is defined by the extent of the electron penetration region. The dominant reducing species is found to be H_2O_2 for this process, which occurs on a time scale dictated by the diffusion time of reducing species transport toward the edge of the electron penetration region. We also show that the expected region of net positive Ag production in the water-ammonia solvent forms a 3D nearly hemispherical region in the quasi–steady state condition. Because of heterogeneous nucleation at the solution-membrane interface, this is manifested experimentally as a ring attached to the membrane. The proposed model of the process could be further enhanced by accounting for the dependence of radiolysis species generation on electron energies; using an electron stopping power model that is more accurate for our range of energies; modeling the kinetics of heterogeneous reactions, solid-phase transport within the liquid deposition domain, and the solid phase's impact on the dose rate distribution; and considering the effects of buoyancy-induced convection on species distributions.

MATERIALS AND METHODS

Experimental results for deposition with 1 mM $AgNO_3$ in both pure water and 30% (v/v) aqueous ammonia solutions are shown in Fig. 2. Experiments were conducted in an FEI Quanta 250 FEG scanning electron microscope using QuantomiX WETSEM QX102 capsules. The solution is enclosed within an electron transparent polyimide membrane and irradiated with electrons of different energies for 30 s.

SUPPLEMENTARY MATERIALS

Supplementary material for this article is available at https://science.org/doi/10.1126/sciadv.abj8751

REFERENCES AND NOTES

1. I. Utke, A. Gölzhäuser, Small, minimally invasive, direct: Electrons induce local reactions of adsorbed functional molecules on the nanoscale. *Angew. Chem. Int. Ed.* **49**, 9328–9330 (2010).
2. I. G. Gonzalez-Martinez, A. Bachmatiuk, V. Bezugly, J. Kunstmann, T. Gemming, Z. Liu, G. Cuniberti, M. H. Rümmeli, Electron-beam induced synthesis of nanostructures: A review. *Nanoscale* **8**, 11340–11362 (2016).
3. E. Longo, W. Avansi, J. Bettini, J. Andrés, L. Gracia, In situ transmission electron microscopy observation of Ag nanocrystal evolution by surfactant free electron-driven synthesis. *Sci. Rep.* **6**, 21498 (2016).
4. S. Jesse, A. Y. Borisevich, J. D. Fowlkes, A. R. Lupini, P. D. Rack, R. R. Unocic, B. G. Sumpter, S. V. Kalinin, A. Belianinov, O. S. Ovchinnikova, Directing matter: Toward atomic-scale 3D nanofabrication. *ACS Nano* **10**, 5600–5618 (2016).
5. Z. Wang, Y. Zhang, E. C. Neyts, X. Cao, X. Zhang, B. W. L. Jang, C.-j. Liu, Catalyst preparation with plasmas: How does it work? *ACS Catalysis* **8**, 2093–2110 (2018).
6. J. S. Fisher, P. A. Kottke, S. Kim, A. G. Fedorov, Rapid electron beam writing of topologically complex 3D nanostructures using liquid phase precursor. *Nano Lett.* **15**, 8385–8391 (2015).

7. K. Rykaczewski, A. Marshall, W. B. White, A. G. Fedorov, Dynamic growth of carbon nanopillars and microrings in electron beam induced dissociation of residual hydrocarbons. *Ultramicroscopy* **108**, 989–992 (2008).
8. N. M. Schneider, M. M. Norton, B. J. Mendel, J. M. Grogan, F. M. Ross, H. H. Bau, Electron–water interactions and implications for liquid cell electron microscopy. *J. Phys. Chem. C* **118**, 22373–22382 (2014).
9. M. Bresin, A. Chamberlain, E. U. Donev, C. B. Samantaray, G. S. Schardien, J. T. Hastings, Electron-beam-induced deposition of bimetallic nanostructures from bulk liquids. *Angew. Chem. Int. Ed.* **52**, 8004–8007 (2013).
10. S. Esfandiarpour, L. Boehme, J. T. Hastings, Focused electron beam induced deposition of copper with high resolution and purity from aqueous solutions. *Nanotechnology* **28**, 125301 (2017).
11. G. Schardein, E. Donev, J. Hastings, Electron-beam-induced deposition of gold from aqueous solutions. *Nanotechnology* **22**, 015301 (2011).
12. U. Schindewolf, P. Wünschel, Comparison of solvated electron reaction rates in water and ammonia. *Can. J. Chem.* **55**, 2159–2164 (1977).
13. T. Buttersack, P. E. Mason, R. S. McMullen, H. C. Schewe, T. Martinek, K. Brezina, M. Crhan, A. Gomez, D. Hein, G. Wartner, R. Seidel, H. Ali, S. Thürmer, O. Marsalek, B. Winter, S. E. Bradforth, P. Jungwirth, Photoelectron spectra of alkali metal–ammonia microjets: From blue electrolyte to bronze metal. *Science* **368**, 1086–1091 (2020).
14. J. S. Fisher, P. A. Kottke, A. G. Fedorov, Synthesis of crystalline metal nanomonoliths by e-beam reduction of negatively electrified jets. *Mater. Today Phys.* **5**, 87–92 (2018).
15. J. Hermannsdörfer, N. de Jonge, A. Verch, Electron beam induced chemistry of gold nanoparticles in saline solution. *Chem. Commun.* **51**, 16393–16396 (2015).
16. T. J. Woehl, P. Abellan, Defining the radiation chemistry during liquid cell electron microscopy to enable visualization of nanomaterial growth and degradation dynamics. *J. Microsc.* **265**, 135–147 (2017).
17. T. Kraus, N. de Jonge, Dendritic gold nanowire growth observed in liquid with transmission electron microscopy. *Langmuir* **29**, 8427–8432 (2013).
18. W. W. Mullins, R. F. Sekerka, Morphological stability of a particle growing by diffusion or heat flow. *J. Appl. Phys.* **34**, 323–329 (1963).
19. R. E. H. J. A. Manion, R. D. Levin, D. R. Burgess Jr., V. L. Orkin, W. Tsang, W. S. McGivern, J. W. Hudgens, V. D. Knyazev, D. B. Atkinson, E. Chai, A. M. Tereza, C.-Y. Lin, T. C. Allison, W. G. Mallard, F. Westley, J. T. Herron, R. F. Hampson, and D. H. Frizzell,, NIST Chemical Kinetics Database, NIST Standard Reference Database 17, Version 7.0 (Web Version), Release 1.6.8, Data version 2015.09, National Institute of Standards and Technology, Gaithersburg, Maryland, 20899–8320. Web address: https://kinetics.nist.gov/.
20. H. T. Nguyen-Truong, Modified Bethe formula for low-energy electron stopping power without fitting parameters. *Ultramicroscopy* **149**, 26–33 (2015).
21. A. Bejan, *Convection Heat Transfer* (John Wiley & Sons, 1994).
22. J. Cazaux, Some considerations on the electric field induced in insulators by electron bombardment. *J. Appl. Phys.* **59**, 1418–1430 (1986).
23. E. Strelcov, C. Arble, H. Guo, B. D. Hoskins, A. Yulaev, I. V. Vlassiouk, N. B. Zhitenev, A. Tselev, A. Kolmakov, Nanoscale mapping of the double layer potential at the praphene–electrolyte interface. *Nano Lett.* **20**, 1336–1344 (2020).
24. T.-H. Fan, A. G. Fedorov, Electrohydrodynamics and surface force analysis in AFM Imaging of a charged, deformable biological membrane in a dilute electrolyte solution. *Langmuir* **19**, 10930–10939 (2003).
25. J. C. Joy, S. Luo, An empirical stopping power relationship for low-energy electrons. *Scanning* **11**, 176–180 (1989).

Acknowledgments

Funding: This work was supported by the U.S. Department of Energy (DOE), Office of Science, Basic Energy Sciences (BES), under Award #DE-SC0010729. **Author contributions:** Conceptualization: A.A., P.A.K., and A.G.F. Methodology: A.A., E.C.B., P.A.K., and A.G.F. Software: A.A. Investigation: A.A. and A.G.F. Resources: A.G.F. Writing (original draft): A.A. and E.C.B. Writing (review and editing): A.A., E.C.B., P.A.K., and A.G.F. Visualization: A.A. and E.C.B. Supervision: P.A.K. and A.G.F. Project administration: A.G.F. Funding acquisition: A.G.F. **Competing interests:** The authors declare interests in the following two U.S. patent applications: "Systems and Methods for Electron Beam Induced Processing" (A.G.F.; U.S. patent app. 62/167,596, filed May 2016) and "Systems and Methods for Electron Beam Induced Processing" (A.G.F.; U.S. patent app. 17/223,620, April 2021, divisional filing). The authors declare that they have no further competing interests. **Data and materials availability:** All data needed to evaluate the conclusions in the paper are present in the paper and/or the Supplementary Materials.

Submitted 8 June 2021
Accepted 2 November 2021
Published 17 December 2021
10.1126/sciadv.abj8751